Physics of Plasmas

RESEARCH ARTICLE | MAY 06 2026

Formation and evolution of pair-Alfvén shocks with PIC simulations

J. D. Riordan ; M. E. Dieckmann ; A. Pe'er

Phys. Plasmas 33, 052301 (2026)
https://doi.org/10.1063/5.0296716

Formation and evolution of pair-Alfvén shocks with PIC simulations

Cite as: Phys. Plasmas **33**, 052301 (2026); doi: 10.1063/5.0296716
Submitted: 14 August 2025 · Accepted: 1 April 2026 ·
Published Online: 6 May 2026

View Online Export Citation CrossMark

J. D. Riordan,[1,a)] M. E. Dieckmann,[2,b)] and A. Pe'er[3,c)]

AFFILIATIONS

[1]Department of Physics, University College Cork, Cork T12 K8AF, Ireland
[2]Department of Science and Technology, Linköping University, SE-60174 Norrköping, Sweden
[3]Department of Physics, Bar-Ilan University, Ramat-Gan 5290002, Israel

[a)]Author to whom correspondence should be addressed: dannyriordan@gmail.com
[b)]Electronic mail: mark.e.dieckmann@liu.se
[c)]Electronic mail: peerasa@biu.ac.il

ABSTRACT

We consider the recently discovered *pair-Alfvén shock wave* occurring in collisionless electron–positron plasmas. We perform a series of particle-in-cell studies in one and two dimensions in order to determine the stability conditions for such a shock and the mechanisms which sustain its growth. Building on our previous simulations, which established that these shocks are initially mediated by the Weibel instability before becoming Alfvénic, we demonstrate that the shock is sustained by self-generated Alfvén waves overtaking the shock in the upstream plasma. As a result, growth is only possible when the guiding magnetic field strength, hence the Alfvén speed, is sufficiently small, $\omega_c \lesssim 0.4$ (in normalized units). Furthermore, the production of the waves in the upstream is dependent on a resonance between the Alfvén wave mode and the thermal noise in the plasma, which is inhibited at high magnetization. This explains the conditional absence of this type of shock identified previously.

I. INTRODUCTION

Relativistic jets are known to exist in a great variety of distinct astronomical objects. They are composed of electrons, positrons, and some unknown fraction of ions. These pairs may already exist at the launching of the jet or be produced by photon–photon pair annihilation in the extreme conditions that exist near the jet base, close to a central compact object (e.g., black hole or neutron star).[1–3] This hot, rarefied plasma is often well-approximated as being *collisionless*, i.e., the rate of direct particle–particle interactions is negligible, and the plasma dynamics is mediated primarily through collective interaction with both externally applied and self-generated B-fields. Within this scenario, fluctuations in the flow will lead to internal shocks, which will dissipate kinetic energy and lead to fluctuations in observed lightcurves.[4]

The so-called *pair-Alfvén shock*, as described in our previous work,[5] is a newly discovered type of shock defined by the following: (1) it occurs in plasmas primarily composed of electrons and positrons; (2) it is initially launched by a filamentation instability as the upstream plasma flows into a slower moving medium; and (3) it is sustained in the steady state by Alfvén waves, which are generated upstream and build up at the shock discontinuity. In that work, we described simulation results, which showed the formation of such a shock subject to a specific magnetization level as well as describing its launching mechanism and distinguishing features relative to similar instabilities.

Plasma instability mechanisms cause flow of energy from the fluid motion into plasma waves, and determining which instability dominates in a given environment is an area of an ongoing study. Contingent on the plasma conditions (e.g., densities of the colliding plasmas), there are many relevant instabilities that can lead to the formation of collisionless shocks.[6,7] In the case of a shocked pair plasma as considered in this work, typically the fastest growing mode will be the filamentation instability; however, other modes, such as oblique modes that occur when the net magnetic field is not aligned with the shock normal, can initially outgrow the filamentation mode and preheat the upstream plasma.[8]

The two-stream instability creates a thermal anisotropy, with higher temperature along the collision direction. Furthermore, it is possible that particles, which are emanated by the shock into the upstream region, trigger the growth of additional instabilities, such as the Bell instability.[9,10]

In our previous work,[5] we identified and characterized this kind of shock in the case of a "weak" magnetic field. Here, we extend this by examining more strongly magnetized environments to determine the requisite conditions for the shock's formation and stability. In particular, we consider the conditions under which the shock forms and examine the role of instabilities resulting from the interaction of shock-heated plasma countering-streaming in the inflowing material.

This work is therefore significant in improving our understanding of trans-relativistic, collisionless, pair plasma environments, such as those predicted to occur at the base of relativistic jets in black-hole microquasars,[11] active galactic nuclei,[2] or compact binary millisecond pulsars.[12] In particular, shocks in these environments provide potential sites for efficient first-order Fermi processes[13] and, hence, are of great interest for the investigation of cosmic ray production.[14]

Astrophysical plasma phenomena of this kind are typically studied using particle-in-cell (PIC) simulations. This is because PIC simulations, while computationally expensive, do not rely on heuristic models of the plasma behavior and allow recovering information on the particles and electromagnetic fields directly. We do, however, out of computational necessity, make the approximation of using one- and two-dimensional spatial grids. We assert[5,15] that these reduced-dimensionality simulations still capture the essential physics, and that the results are still qualitatively applicable to real-world 3D scenarios.

Despite this there are notable limitations to the reduced-dimensionality simulations. Some notable drawbacks are: in 1-dimensional simulations, the filamentation instability is inhibited due to the alignment of the simulation box with the magnetic field. As a result, only the two-stream instability contributes to the shock growth, and hence, the shock takes an artificially long time to form. In the 2D geometry, filamentation modes with in-plane magnetic fields are excluded, implying again a slowing of pair-Alfvén shock generation.

This paper is organized as follows. In Sec. II, we discuss the theory of pair-Alfvén shocks. In Sec. III, we discuss the simulation details. Our results are presented in Sec. IV. We discuss our findings and conclusions in Sec. V.

II. BACKGROUND

A. Pair-Alfvén waves in a thermal-equilibrium plasma

Throughout this work, we use naturalized units in order to simplify presentation. Frequencies are normalized to the total pair plasma frequency $\omega_p = \sqrt{2}\omega_{pe}$, where ω_{pe} is the plasma frequency of electrons with density n. Time is, therefore, given in units ω_p^{-1}. This further implies that the frequency is given in units of ω_p. We normalize distance to the skin depth $\lambda_s = c/\omega_p$. Electric fields $\mathbf{E}$ are normalized to $m_e c\omega_p/e$ and magnetic fields $\mathbf{B}$ to $m_e\omega_p/e$, where c is the speed of light, e is the electron charge, and m_e its mass.

The dispersion relation for a wave in a warm, magnetized pair plasma was derived by Keppens *et al.*[16] [their Eq. (4.2)]. This equation, when written in natural units, reads

$$\omega^6 - \omega^4\left(B^2 + k^2 v_s^2 + k^2 + 2\right) - \omega^2\left(-B^2k^2\Lambda^2 v_s^2 - B^2k^2 - B^2 - k^4v_s^2 - k^2v_s^2 - k^2 - 1\right) - B^2k^4\Lambda^2v_s^2 - B^2k^2\Lambda^2 = 0. \quad (1)$$

Here, ω is the wave frequency, B is the magnetic field strength, $\mathbf{k}$ is the wavevector, $k = |\mathbf{k}|$ is the wavenumber, v_s is the plasma sound speed, and the wave orientation relative to the magnetic field is measured by $\Lambda = \mathbf{k}\cdot\mathbf{B}/kB$. The sound speed v_s can be taken as 0 for a cold plasma.

We assume the presence of a "background" magnetic field $\mathbf{B}_0$ with the amplitude $B_0 = |\mathbf{B}_0|$, and we orient our coordinate system such that it is aligned with the x axis. Components of particle velocity and wavevectors parallel and perpendicular to this field will be denoted as $v_\parallel, k_\parallel$ and $v_\perp, k_\perp$, respectively.

Although, in general, there exist six different wave solutions, by taking $\mathbf{k} \parallel \mathbf{B}_0$ and hence $\Lambda = 1$, we recover the familiar Alfvén solution,

$$\omega = \Lambda kB/\sqrt{1+B^2} = v_A k,$$

where $v_A = B/\sqrt{\mu}$ is the non-relativistic Alfvén speed and μ is the charge density. We focus on the low-frequency regime in which only this pair-Alfvén wave exists.

In the limit of low k, cold pair Alfvén waves have phase speed $v_\phi = \omega/k = B_0/(2\mu_0 n m_e)^{1/2}$, where μ_0 is the vacuum permeability. The charged particles gyrate at the normalized electron gyrofrequency, $\omega_c = eB_0/\omega_p m_e$. In the limit of high wavenumber k and $\omega_c < 1$, the wave frequency converges to ω_c, the cyclotron resonance.[16]

Particles will resonate with pair-Alfvén waves if they meet the resonance condition: $\omega = \omega_c \pm \mathbf{v}\cdot\mathbf{k}$. In our simulations, the highest energy particles drawn from the thermal distribution have a speed approximately $4v_t$ (where $v_t = \sqrt{k_B T_e/m_e}$ is the thermal speed and T_e is the electron temperature), and this determines the range of velocity angles for which resonant interaction can occur.

B. Two-stream and firehose instability

As established in our previous work,[5] structures are seen to form in the density distributions corresponding to electrostatic "holes" in phase space, i.e., localized areas with relatively low or zero density. The observed structure in the downstream region results when these phase space holes collapse and disappear. While the holes can be stable in 1D simulations, they eventually collapse in higher dimensions. These collapses heat the plasma and, thus, serve to transfer energy from the counterstreaming beams into isotropic thermal motion. In that work, we found the holes are present until $t \approx 500$ (here and throughout references to times in the simulation are given in our normalized units) when they are disrupted by the growth of the pair-Alfvén waves.

We note two distinct regions of the plasma with counterstreaming beams, which give rise to a two-stream instability (see sketch in Fig. 1). First, in the overlap layer, we have beams flowing into and out of the shock with almost identical properties. In the upstream, we have a dense beam as well as a shock-heated pair component. Hence, we expect to find two distinct scenarios for pair-Alfvén instability growth corresponding to each of these regions.

Firehose-type instabilities are produced at parallel shocks when a threshold number of particles with $v_\parallel \approx \omega/k_\parallel$ is reached, and an anisotropic velocity distribution is present.[17–19] It will be useful to define the parallel and perpendicular temperatures, $T_\parallel = T_x$ and $T_\perp = T_y + T_z$. These refer to the temperature in two orthogonal

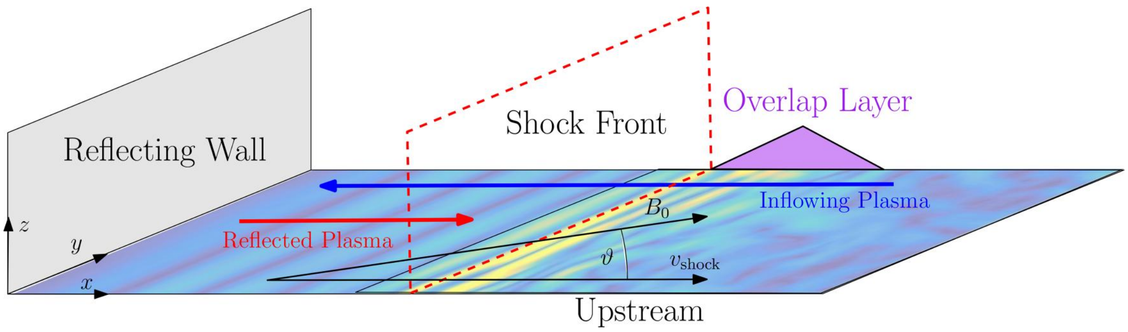

FIG. 1. Sketch of simulation domain. We distinguish the following sub-regions: *overlap layer*—where the inflowing plasma and the plasma reflected from the left wall meet upstream, here the plasma is cold in the fluid frame; *downstream*—expanding from $x = 0$, this region contains the plasma, which has been processed by the shock and is dense and hot in all directions; *foreshock*—the region where energetic particles have escaped from downstream and the overlap layer and interact with the inflowing upstream plasma. The foreshock is not labeled here but extends from the right of the overlap layer into the upstream. Note the z dimension is not resolved, and that in the 2D simulations, where the y dimension is resolved, we have used a periodic boundary condition.

projections of the full 3-dimensional spatial domain, the first a line parallel to the shock normal and the other a plane-parallel to the shock plane, such that the total temperature is given by $T = T_\perp + T_\parallel$. The anisotropy condition is (for the downstream) $T_\perp/T_\parallel < 1 - 1/\beta$, where $\beta = 2\mu_0 n k_B T/B^2$ is the ratio of kinetic to magnetic pressure, and k_B is the Boltzmann constant. We can restate this in terms of the ratio of Alfvén (v_A) and thermal speeds,

$$\frac{T_\perp}{T_\parallel} < 1 - \frac{\mu_0}{2}\frac{v_A^2}{v_t^2}. \tag{2}$$

Since these firehose modes depend on the presence of a thermal anisotropy, they will be quenched if the plasma distribution is returned to isotropy, for example, by a separate instability. As we will show, this can occur in the downstream of the environments considered in this work where the two-stream instability will thermalize the plasma along x. The aforementioned analysis cannot be applied to the foreshock, since it cannot be well-approximated by a single distribution with different parallel and perpendicular thermal speeds. In this case, a fully kinetic treatment is possible,[20] and the anisotropy condition $T_\perp \neq T_\parallel$ is replaced by

$$(\omega - k_\parallel v_\parallel)\frac{\partial f}{v_\perp \partial v_\perp} \neq k_\parallel \frac{\partial f}{\partial v_\parallel},$$

where f is the momentum distribution function.

III. SIMULATIONS

A. Theory

We use the plasma physics simulation code EPOCH.[21] This code numerically solves Maxwell's equations on a fixed grid to time-evolve a relativistic system of electromagnetic waves and charged particles. For this task, it uses an explicit second-order scheme, the particle in cell (PIC) method.[22] In the PIC method, collections of physical particles are represented using a smaller number of "pseudoparticles," and the fields generated by their motion are calculated using a leapfrog finite-difference time-domain (FDTD) method. The forces on the pseudoparticles due to the calculated fields are then used to update the pseudoparticle position and momentum using the Boris Pusher scheme.[21] EPOCH is capable of accurately simulating a large variety of plasma systems at the microphysical scale.[21]

Ampère's law $\mu_0\epsilon_0\dot{\mathbf{E}} = \nabla \times \mathbf{B} - \mu_0\mathbf{J}$ and Faraday's law $\dot{\mathbf{B}} = -\nabla \times \mathbf{E}$ are approximated on a numerical grid, where $\mathbf{E}$, $\mathbf{B}$, and $\mathbf{J}$ are the electric field, the magnetic field, and the current density, respectively, and ϵ_0 is the vacuum permittivity. Each plasma species j is approximated by an ensemble of computational particles (CPs). The ith CP has a charge-to-mass ratio q_i/m_i that must match that of the species j it represents. The electromagnetic fields are coupled to the CPs, and the CPs are coupled to $\mathbf{J}$ via suitable numerical schemes as implemented in the EPOCH code we use.[21]

B. Numerical setup

Our simulation begins with an isotropic electron–positron plasma, both species have densities $n_0/2$ and temperature $T_0 = 10\,\text{keV}$, which gives thermal velocity $v_t = 0.14c$.

In the 1D simulations, we resolve a box length $L_N = 2800$ (in simulation units normalized to λ_s) by 2×10^4 simulation cells and each particle species by 100 particles per cell. The cell size is therefore equal to the Debye length $\Lambda_D = v_t/\omega_p = 0.14$ and smaller than the skin depth by a factor of ≈ 7. The code runs until the simulation time $t_{\text{sim}} = 4 \times 10^4$ is reached, which was observed to be long enough to allow for transient effects. To ensure that the box size is sufficiently large, we further perform an additional 1D simulation with the same plasma parameters, using 10^7 CPs for each species. The simulation box length is $L_x = 21\,270$, which we resolve by 148 000 cells. The grid cell size is then $\Lambda_D \approx \lambda_s/7$ as before.

Our two-dimensional simulations resolve x by 2×10^4 grid cells and y by 2000 grid cells. Boundary conditions are reflective along x and periodic along y. We model one electron species and one positron species, which are uniformly distributed in space. Each species has a density $n_0/2$ and simulated by a total of 8×10^8 CPs.

The simulation box spans the intervals $0 \le x \le 2650$ and $0 \le y \le 265$, which are likewise in simulation units normalized to λ_s. Both species have a Maxwellian velocity distribution with temperature $T_0 = 10\,\text{keV}$, which gives the thermal speed $v_t = 4.2 \times 10^7\,\text{m/s}$. The bulk fluid speed is $v_d = -3v_t$ along x (which corresponds to 0.42c in the simulation). The Debye length is $\Lambda_D = 0.14$. A magnetic field $\mathbf{B}_0 = B_0(\cos\vartheta, \sin\vartheta, 0)$ is present at $t = 0$. B_0 is determined by the

TABLE I. Representative values of plasma parameters in the simulated system for $\omega_c = 0.1$.

Cell size	d_x	8.00×10^1 m
Total electrons	N_e	1000
Number density	n_0	$1.66 \times 10^8/\mathrm{m}^{-3}$
Guide B-field	B_0	4.48×10^{-7} T
Alfvén speed	v_A	3.24×10^7 m/s
Plasma frequency	ω_p	7.28×10^5 Hz
Skin depth	λ_s	4.11×10^2 m
Wave scale	k_0	2.43×10^{-3} m^{-1}
RMS momentum	p_0	1.20×10^{-22} kg m/s
Drift momentum	p_d	1.14×10^{-22} kg m/s
Drift Lorentz factor	γ_d	1.08
Drift velocity	v_d	1.15×10^8 m/s
Alfvén Mach number	M_A	3.54
Initial temp.	T_0	1.16×10^8 K
Drift momentum	p_{drift}	1.14×10^{-22} kg m/s
Thermal velocity	v_0	5.92×10^7 m/s
Gyroradius (for B_0)	r_g	1.06×10^3 m

choice of the electron gyro-frequency parameter $\omega_c = eB_0/m_e\omega_p$ (numerically, both B_0 and ω_c are identical when expressed in the code's normalized units). The pair-Alfvén speed $v_A = B_0/(\mu_0 n_0 m_e)^{1/2}$ is then $0.7v_t$ ($0.1c$) in the $\omega_c = 0.1$ case. The 2D simulations are stopped at $t_{\mathrm{sim}} = 2500$ (in simulation units). We checked that this time is sufficiently long to capture all transient effects of interest. Parameter values are given for the $\omega_c = 0.1$ case in SI units in Table I.

In total, we perform four simulations of a parallel shock in 1D (varying ω_c), three in 1D for oblique shocks (varying the angle between the shock and the background field ϑ), and finally four 2D simulations varying ω_c as in the first set. In this way, we are able to observe what effects the limitations of the (computationally simpler) 1D simulations have on the shock dynamics and understand how the shock obliquity affects the results. Finally, we fulfill our primary goal of extending our prior work[5] to higher magnetic fields and describing the different regimes of pair-Alfvén shock behavior.

IV. RESULTS

A. Initial shock formation

In Fig. 2, we plot the early-time results of our 1D simulation in order to examine the initial shock formation process for four values of the electron gyro-frequency: $\omega_c = 0.1, 0.2, 0.4$, and 0.8. The corresponding Alfvénic Mach numbers $M_A = v_d/v_A$ are 3.54, 1.77, 0.89, and 0.44, respectively. From the figure, one sees a clear qualitative distinction in the shock formation processes. In the $\omega_c = 0.1, 0.2$ cases (left panels), a distinct initial period during which the counterstreaming plasma has not yet developed is observed, until approximately $t = 5 \times 10^2$, 3×10^2, respectively.

During this phase, the shock grows as pair-Alfvén waves accumulate at the shock front (which we will see in Fig. 5), and a charge separation is apparent in the lower panels. As discussed in Dieckmann *et al.*,[3] this charge separation is a result of the oscillating

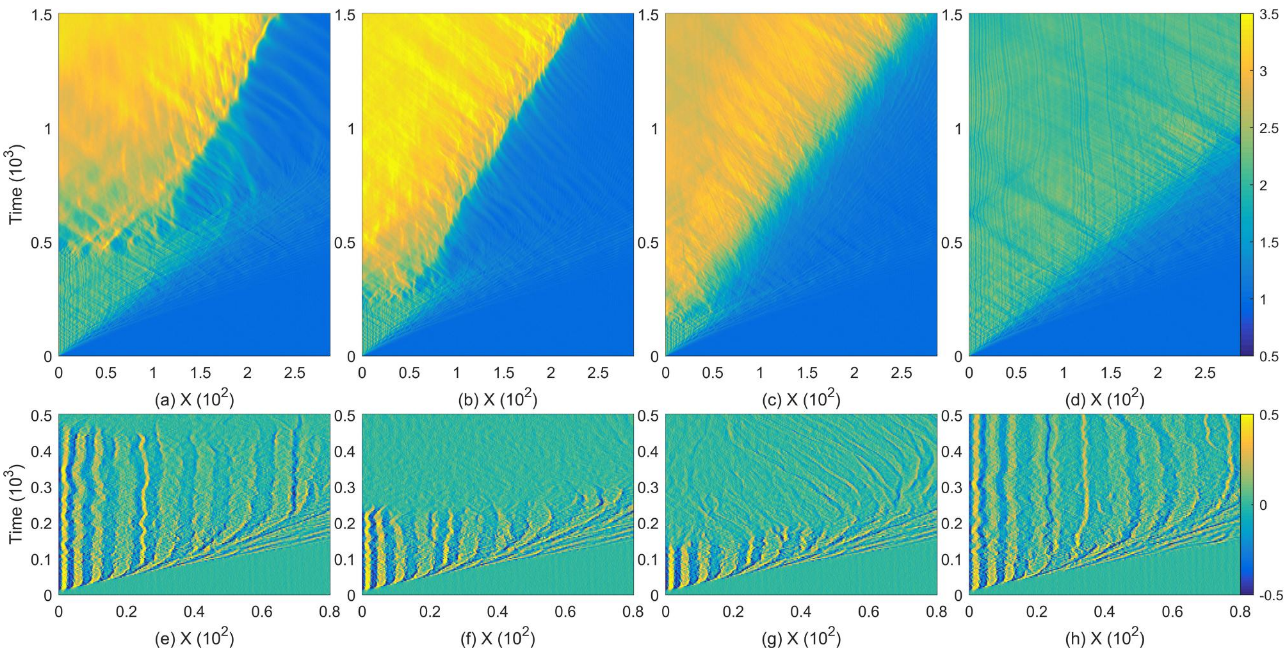

FIG. 2. Initial evolution of the plasma in and near the overlap layer, showing the number density (upper panels) and charge separation (lower panels) as functions of space (x-axis) and time (y-axis). Panel (a) shows the electron number density n_{e^-} in the simulation with $\omega_c = 0.1$, (b) that in the simulation with $\omega_c = 0.2$, (c) that in the simulation with $\omega_c = 0.4$, and (d) that in the simulation with $\omega_c = 0.8$. Panels (e)–(h) show the difference $n_{e^+} - n_{e^-}$ between the number densities of positrons and electrons corresponding to the cases earlier. Panel (e) shows the difference for $\omega_c = 0.1$, (f) that for $\omega_c = 0.2$, (g) that for $\omega_c = 0.4$, and (h) that for $\omega_c = 0.8$.

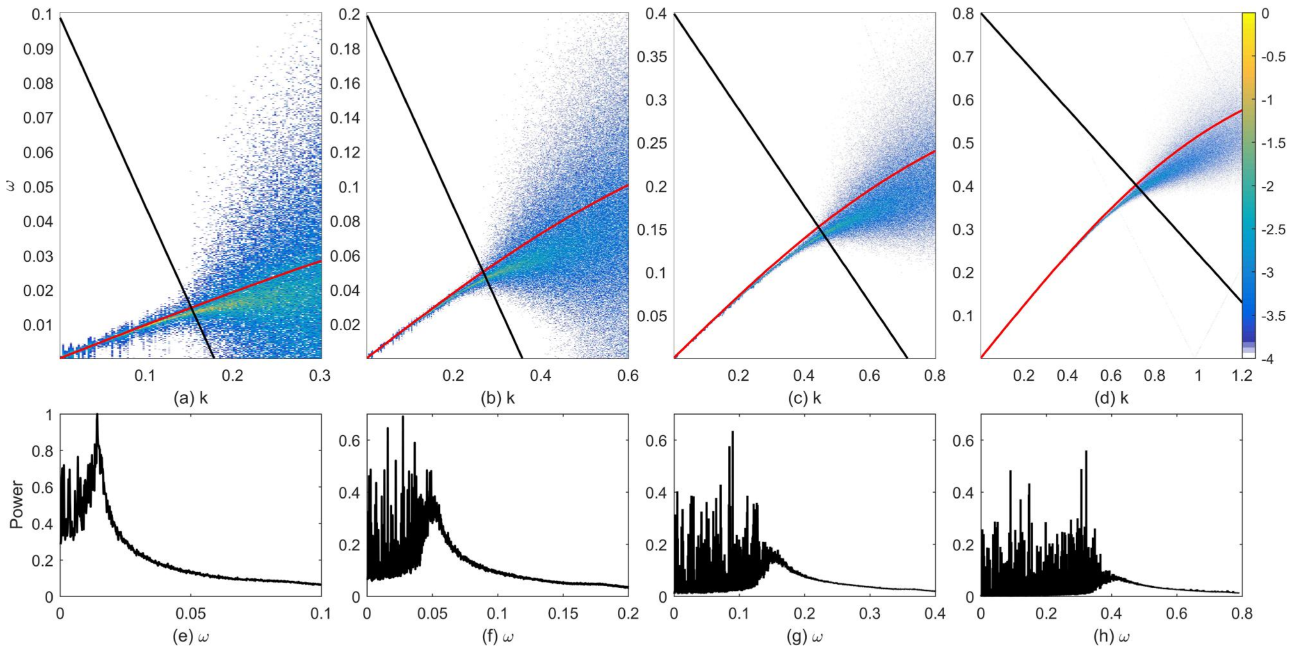

FIG. 3. Power spectrum of *B*-field in 1D simulations for wave vectors parallel to the background magnetic field $\mathbf{B}_0$, along with the dispersion relation of pair-Alfvén mode (red) and line separating areas of low and high damping (black). Panels (a) and (e) correspond to the case $\omega_c = 0.1$. Panels (b) and (f) correspond to $\omega_c = 0.2$. Panels (c) and (g) correspond to $\omega_c = 0.4$. Panels (d) and (h) correspond to $\omega_c = 0.8$.

E_x at the shock front. Once this process is complete, the shock will have reached a steady state and efficiently thermalizes the downstream leaving a homogeneous plasma behind.

In the third column ($\omega_c = 0.4$), one observes a similar behavior; however, the downstream plasma retains some minor charge separation, and the shock front is less sharp. Finally, in the $\omega_c = 0.8$ case, the formation of the shock is suppressed, and no clear shock is observed to form.

This is explained by noting that the range of thermal anisotropy values which are stable with respect to the mirror instability shrinks with increasing plasma β as (see Ref. 7)

$$1 - 1/\beta \leq T_\perp/T_\parallel \leq 1 + 1/\beta. \tag{3}$$

As a result, the range of anisotropy values for which the mode is unstable and produces Alfvènic turbulence shrinks while $\omega_c \propto \beta^2$ increases.

Temperature anisotropy, $T_\perp/T_\parallel \neq 1$, may arise from heating of plasma, which is permeated by a uniform background magnetic field. The magnetic field gives rise to different particle mobilities perpendicular and parallel to the magnetic field. Wave properties depend on the angle between their wave vector and the magnetic field direction. Hence, the heating of particles in collisionless plasma, like the one by the waves driven by two-stream instability or shock waves, often introduces thermal anisotropies. These anisotropies can then relax through mirror instabilities and firehose instabilities.[3]

B. Wave spectra

In order to examine the energy distribution in the Alfveńic modes, we take the unshocked uniform plasma and Fourier transform the magnetic field energy density $B^2(x,t)$, as recorded over the full spatial and temporal range of the simulation, to $k-\omega$ space. The logarithm is plotted in Figs. 3(a)–3(d), normalized to the respective maxima.

We overplot two lines, and the red line gives the analytic solution for pair-Alfvén wave with the parallel magnetic field.[16] The black line shows $\omega = \omega_c - v_t k$, which is the threshold for resonant interaction with the charged particles and, hence, delimits the region where the waves will be damped and deviate from the ideal wave solution. We find a sharp wave branch only to the left of this line, demonstrating good agreement with the expected Alfvén solution. Waves to the right of the black lines, while still following the analytical dispersion relation, interact strongly with particles and become increasingly damped as k is increased.

We obtain the power spectral density by integrating over all k at each ω and display the results in Figs. 3(e)–3(h). When increasing the magnetic field, hence cyclotron frequency ω_c (from left to right in Fig. 3), the dispersion relation is modified, and the red lines become steeper. This results in a broadening of the observed spectrum [see panels (e) to (h)] and, hence, a broader range of velocities of Alfvén wave propagation. This weakens the condition of matching the Alfvén speed to the shock speed since waves at higher k will be slowed. The noise power peaks at the frequency, where the waves start interacting with the particles, and decreases steadily as we increase the frequency to ω_c.

This setup also allows us to study the wave properties for the oblique case. We perform simulations taking the same parameters as above but rotating the magnetic field with strength $\omega_c = 0.8$ by each of 30°, 45°, and 60° in the xy plane. The results are plotted in Fig. 4. The power has been normalized to the peak value for each of the three

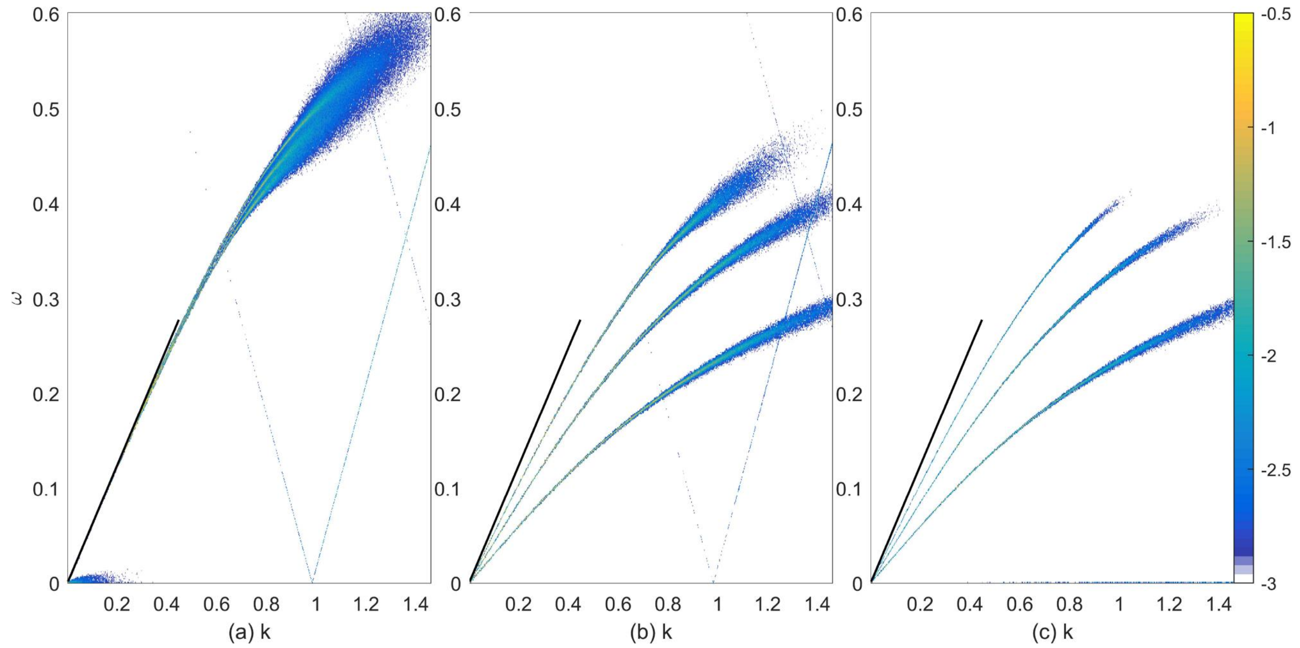

FIG. 4. Panels (a), (b), and (c) show the power spectrum of waves in B_y, B_z, and E_x, respectively. We have merged the results for obliquity angles $\vartheta = 30^\circ$, 45°, and 60° (relative to the x axis). The branches overlap in (a) and can be identified in (b) and (c) by noting that increasing ϑ results in a decrease in the slope near the origin (i.e., the phase velocity). Panel (a) shows $\log_{10}(B_y^2/B_{\max}^2)$, (b) shows $\log_{10}(B_z^2/B_{\max}^2)$, and (c) shows $\log_{10}(E_x^2/c^2B_{\max}^2)$, where $B_{\max}^2 = \max B_y^2$ is the peak of the power in the y-component of the B-field. The overplotted black line corresponds to the dispersion relation $\omega = v_A$ of the $\alpha = 0$ Alfvén wave. The diagonal structures with low power are high-frequency $\omega \gg \omega_p$ modes that have been aliased due to the limited data sampling rate.

simulations, and all three power spectra have been shown together to allow for direct comparison.

The waves shown in Fig. 4(a), which correspond to the power in B_y, change the amplitude of the background magnetic field; we identify them as fast magnetosonic waves. As such, their propagation does not depend on a background magnetic field parallel to the wavevector, as is the case for Alfvénic modes. Their phase speed matches the Alfvén speed for $k < 0.4$, and it hardly changes with the propagation angle in this k-interval. Note that these modes do not exist when $\alpha = 0$ (wave vector parallel to $\mathbf{B}_0$).

In contrast, for the waves in Fig. 4(b), we observe the expected $\cos\alpha$ decrease in wave speed as well as an increased deviation from the expected result at a higher wavenumber in the case of higher obliquity. These modes have a magnetic field component orthogonal to $\mathbf{k}$ and $\mathbf{B}_0$ and their phase speed at low k is $v_A \cos\alpha$. We identify them as oblique pair-Alfvén waves. These waves may have an electrostatic component, as is the case for our chosen plasma parameters [see Fig. 4 panel (c)]. The figure shows a clear concentration of electromagnetic (EM) power in these normal and oblique modes.

In what follows, we consider only the parallel case, as this is most likely to produce a shock, and aside from the points discussed earlier, the long-term evolution of the oblique shocks did not demonstrate any materially different results.

C. Long-term evolution of the 1D shock

We next consider the steady state configuration of the shock formed. In Fig. 5, we show the phase space density distribution, the density and the square root of the normalized magnetic pressure $P_B = ((B_x - B_0)^2 + B_y^2 + B_z^2)/2\mu_0$ for the three cases considered here ($\omega_c = 0.2, 0.4,$ and 0.8) at time $t = 10^4$, where the generated shocks reach a (quasi-) steady state. At a stronger magnetic field, the Alfvén speed is higher; hence, the shock speed is higher, and the shock propagates faster, as can be seen in the figure [panels (a) and (b)].

At lower magnetic fields, more Alfvénic waves are accumulated near the shock front, implying a sharper discontinuity of the fluid properties at the front [panels (c)] as well as stronger magnetic pressure [panels (d)]. This amplification of the waves due to compression by the shock is expected since the Alfvén speed is inversely proportional to the number density of charge carriers, $v_A \propto n^{-1}$. Furthermore, the compression ratio across the shock is seen to decline with increasing ω_c, as expected.[17–19] In addition to the smoothed shock front, we note distinct differences in the extent of the foreshock, seen in panels (a) and (b) as the region ahead of the shock with a population of heated particles outside the original upstream distribution.

From Fig. 5, one can discern distinct regimes of shock behavior as a function of the cyclotron frequency ω_c. The shock formed in the presence of a weaker magnetic field, $\omega_c = 0.2$, is slowest, its density is highest, and the magnetic pressure is located primarily at the shock. With increasing background field strength, one sees smoothing of the discontinuity as well as more pronounced anisotropy in momentum space. For the strongest magnetic field ($\omega_c = 0.8$), no Alfvénic shock is formed, as can be seen by the factor 2 in the density jump.[19] This may, however, indicate a one-dimensional electrostatic shock,[23] and it is possible that as phase space holes collapse, a shock could be launched at a later time.

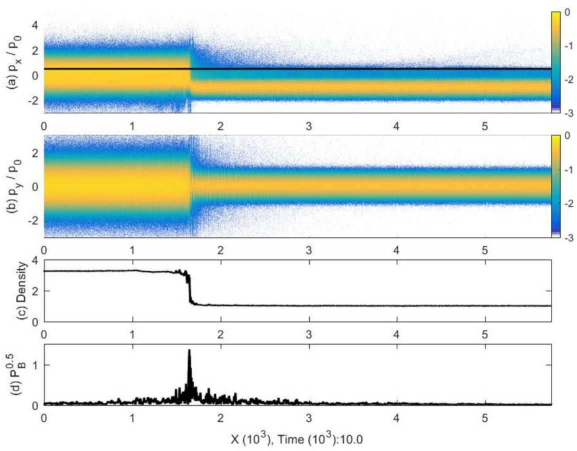

(i) $\omega_c = 0.2$

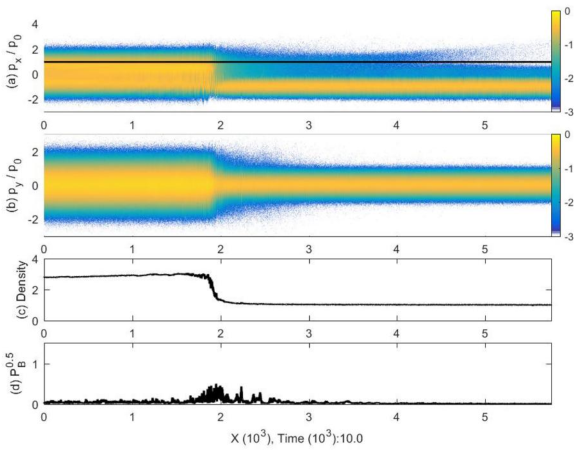

(ii) $\omega_c = 0.4$

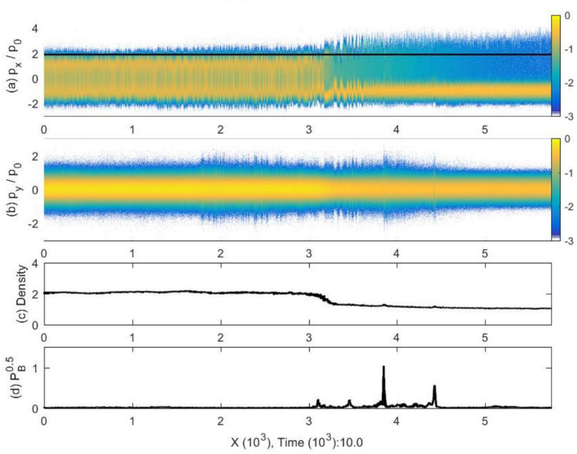

(iii) $\omega_c = 0.8$

FIG. 5. 1D simulation results at $t = 10^4$ for different values of ω_c. (a) and (b) The phase space log-density distributions $\log_{10} f(x, p_x)$ and $\log_{10} f(x, p_y)$, normalized to p_0, the peak value at $t = 0$. (c) The total number density in units of $n_0/2$, while (d) shows $P_B^{1/2}$. The black horizontal line in the top panel marks $p_x/p_0 = m_e v_A$.

In Fig. 6, we show the momentum distribution functions of the electrons and positrons in the region $0 < x < 10^3$, comparing the initial and intermediate ($t = 1336$) states. From these, one can see how the distributions, which are initially thermal with equal temperature in each direction, have been modified by interaction with the shock and the associated magnetic turbulence. We examine each of the three cases $\omega_c = 0.2, 0.4, 0.8$ to assess the effect of each magnetic field strength on the timescale for relaxation to thermal equilibrium. Since anisotropic velocity distribution is the source of the Alfvénic turbulence, this figure demonstrates the time evolution of the wave growth rate.

The simulation state in Fig. 6(a) has reached approximate equilibrium. The equilibrium is not complete, since there is a small deviation in the p_x distribution; however, otherwise, we observe the entropy-maximizing case of a thermal and isotropic distribution. The increase in the enclosed area for the final curves represents a higher particle count in the considered region due to the compression of the plasma in the downstream.

The state shown in Fig. 6(b) is still evolving toward an equilibrium; the blue curve shows peaks in the incoming and reflected velocity direction, but the blue peak at negative p_x is at a lower speed than the initial beam mean speed. The perpendicular direction has also been heated, which is evidenced by the flatter distribution.

Figure 6(c) is clearly far from equilibrium. The red curve is approximately double the initial distribution because incoming and reflected beams have been added together, but similar same mean speed and temperature are seen along that direction. The peaks of the blue curve are located at $p_x \approx \pm m_e v_0$.

Further simulations were performed for oblique shocks (as in Fig. 4), and no discernible difference was seen in their long-term evolution.

Particles that leak from the overlap layer into the foreshock are both hot and anisotropic, leading to a firehose instability.[20] This is a result of the broad distribution of $v_\parallel$. The waves in the $\omega_c = 0.8$ case escape upstream and away from the boundary overlap layer and foreshock.

Building on our previous conclusion[5] that $\omega_c = 0.1$ rapidly leads to equilibration, we find the following: the configuration with $\omega_c = 0.2$ likewise converges rapidly, $\omega_c = 0.4$ does so more slowly but notably in our results, and $\omega_c = 0.8$ does not appear to reach an equilibrium within the time considered. These results provide an approximate answer to our initial research question regarding the effect of the background field on the formation and stability of the pair-Alfvén shock.

D. 2D simulations

In Sec. IV C, we have shown in the 1D simulations that the largest magnetic field suppresses the formation of a shock and excludes all wave modes not satisfying $\mathbf{k} \parallel \mathbf{x}$. Here, we extend the analysis by considering 2D simulations of the same environment, in order to examine if the same suppression occurs.

In Fig. 7, we plot the magnetic field distribution near the shock at time $t = 1336$, for the case $\omega_c = 0.2$. The amplitudes of the magnetic field components are comparable to that of B_0, and the waves are, thus, well into the nonlinear regime. The pair-Alfvén wave is practically planar. As in the 1D case [panels (d) in Fig. 5], we can see a concentration of magnetic energy in the vicinity of the shock front, at

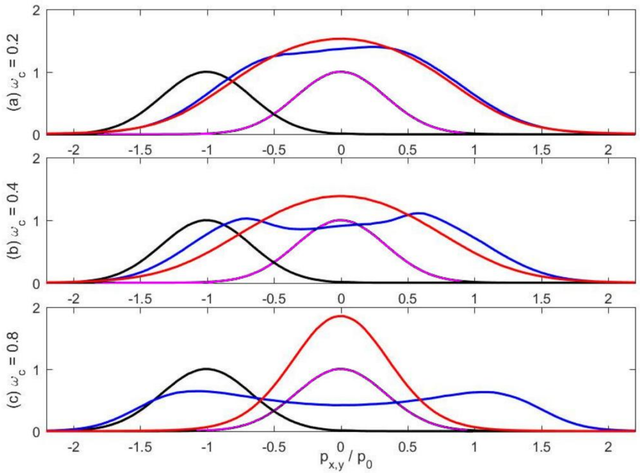

FIG. 6. Momentum distributions averaged over $x < 10^3$: (a) the simulation with $\omega_c = 0.2$, (b) the simulation with $\omega_c = 0.4$, and (c) the simulation with $\omega_c = 0.8$. The black curve shows the initial plasma distribution along p_x, and the purple corresponds to p_y. Blue and red curves show the distributions at $t = 1336$ along p_x and p_y. All curves are normalized to the peak value of the initial distribution. Due to the particle flow, the later curves contain more particles and, therefore, cover a larger area than the initial curves.

$x \approx 200$; see panel (c). Also similarly to the 1D case, the shock is much faster than the waves, which results in the accumulation of magnetic energy at the shock front, which is amplified as it crosses the discontinuity and is compressed.

The y-averaged phase space density distribution is shown in Fig. 8(i), with downstream and upstream regions separated by a sharp transition layer. A population of energetic particles is moving upstream, as is seen in Fig. 8(i-a) (left side of the figure). Their momenta perpendicular to the flow direction are relatively small, since they originate from a thermal distribution, and only those whose momentum lies mostly along **x** can outrun the shock. Particles shown in panels (b) and (c) move on helical orbits under the influence of the magnetic field. They have a large wavelength upstream, which is diminished after crossing the shock due to the relatively stronger background magnetic field.

The results obtained with $\omega_c = 0.8$ [Fig. 8(ii)] show the same phase space density distribution as in Fig. 8(i) but this time for the strong magnetic field case. As opposed to the results seen in Fig. 8(i), no shock appears in Fig. 8(ii), as is evident from the fact that no sharp discontinuity in the particle momentum is observed.

The downstream plasma is cooler along y and z than along x, and the distribution as seen in Fig. 8(ii-a) is non-Maxwellian. The shape of the distribution exhibits electrostatic phase space holes. This represents a plasma transition layer that is not bounded by a shock.

The magnetic field distributions in Fig. 9 show clearly distinguished waves in the xy plane. In contrast to the $\omega_c = 0.2$ case, we see a smooth change in density along x with no clear shock front. We also observe a periodic variation in y, implying a spontaneous generation of oblique waves. Although this variability was present in the lower ω_c cases, it was not pronounced because the presence of the shock wave implied that these relatively small fluctuations were dominated by waves oriented along the x (shock propagation) direction. The box size along y is large enough to resolve one wave oscillation along this direction.

Having $k_y \neq 0$ implies the presence of spontaneously generated oblique waves (distinct from the 1D case, where obliquity was imposed by rotating the background field). These waves have their speed reduced by a factor of $\cos \alpha$ and cannot outrun the expanding

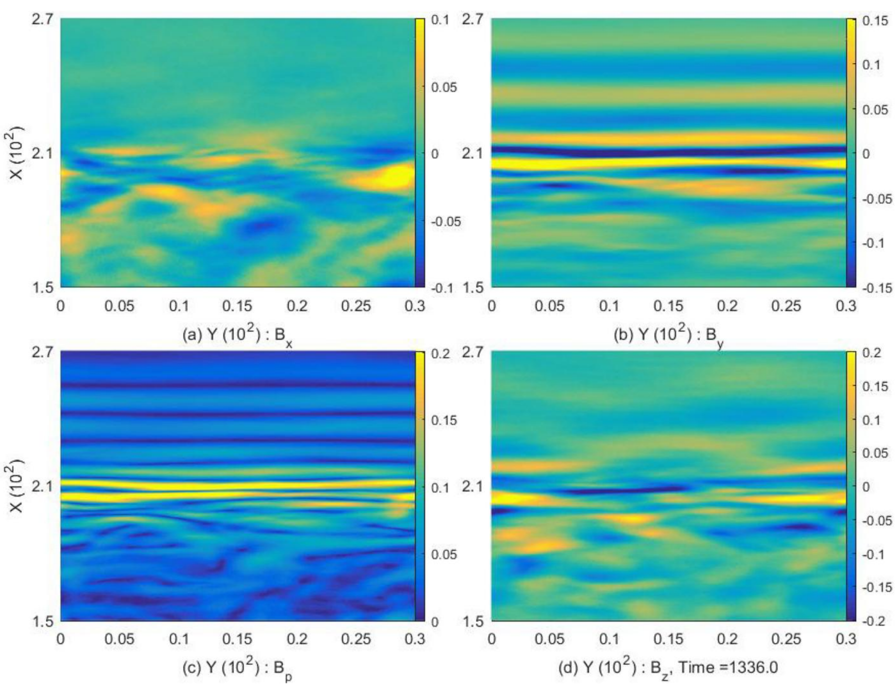

FIG. 7. Magnetic field distribution near the shock for $\omega_c = 0.2$ and $t = 1336$: (a) the magnetic B_x component. (b) B_y. (c) $B_p = ((B_x - B_0)^2 + B_y^2)^{1/2}$ and (d) B_z. In the normalized units we use here, the maximum value of the magnetic field is 0.2, similar to B_0.

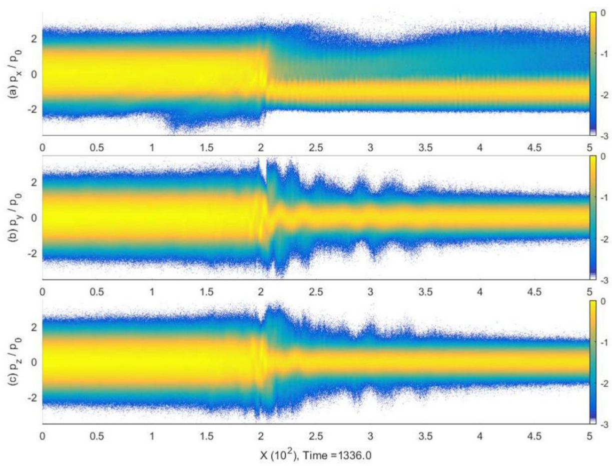

(i) $\omega_c = 0.2$

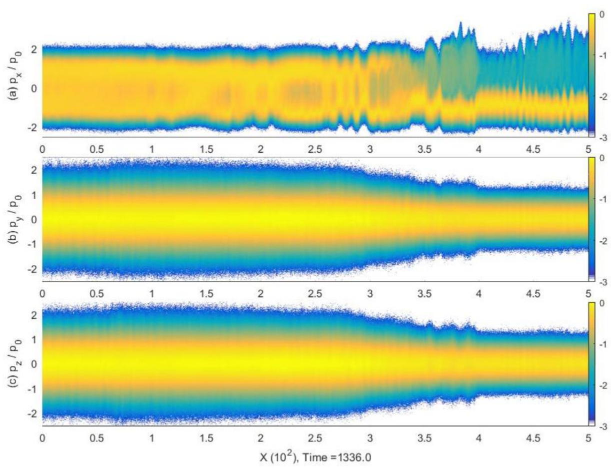

(ii) $\omega_c = 0.8$

FIG. 8. Phase space density distribution at the time $t = 1336$ for different values of ω_c. All distributions have been averaged over y. (a) The projection of the distribution onto the x, p_x plane. (b) and (c) The projections onto the two other momentum directions. Phase space densities are normalized to their initial peak value and displayed on a base-10 logarithmic scale.

plasma, cf. Fig. 4. Their amplitude is much lower than that of the corresponding waves for the lower magnetization case shown in Fig. 7 because the Alfvén waves are too fast to accumulate at the shock front. We also see fast magnetosonic waves, but they are not well-structured.

We also repeated the simulation with a y-scale increased by a factor of 10, to examine the possibility of spurious effects arising from the small size relative to the wavelength of these observed fluctuations. The results appear similar in the simulations with the original and larger boxes, in particular the wavelength was not affected. This indicates that although the computationally convenient assumption of a periodic boundary along y is unphysical, it does not significantly affect the outcome. We do notice a slightly stronger B_z, but this might be coincidental and does not invalidate our conclusions.

The degree to which the Alfvén wave thermalizes the plasma determines the speed of the shock. If significant energy is transferred into the perpendicular degrees of freedom of the particles, then the compression ratio will be higher and, hence, the shock speed will be lower.

In contrast to the case discussed in Sec. II B, the overlap layer for the $\omega_c = 0.8$ case is not firehose-unstable. Furthermore, the $\omega_c = 0.4$ case appears to lie close to the stability threshold.

V. DISCUSSION

In this work, we studied the formation of Pair-Alfvén shocks in the presence of range background magnetic field strengths. These discontinuities had previously been identified only in simulations with magnetization corresponding to the "weak" case in this work.[3] We have used the terms "weak," "intermediate," and "strong" here in a relative sense; we note that in other astrophysical contexts, they may all be considered strong fields. Using both 1D and 2D simulations with the PIC code EPOCH, we identify the upper magnetization threshold beyond which these shocks cannot form, explain the suppression mechanism via anisotropy-inhibited Alfvén wave growth, and distinguish three distinct regimes of shock behavior based on the magnetic field strength. It also confirms that oblique Alfvén modes, which cannot appear in 1D, do not compensate for this suppression. Hence, we have provided new constraints on shock formation in such collisionless pair plasmas as are expected to be produced at, e.g., the base of jets.

Our particle-in-cell simulations demonstrate that these recently discovered pair-Alfvén shocks are sustained by self-generated Alfvén waves that overtake the shock front in the upstream plasma. The simulations show that the shock only develops when the background magnetic field and associated Alfvén speed are sufficiently low to enable this wave amplification process. At higher magnetizations, our results indicate the Alfvén wave growth is suppressed, and the increased speed means that waves outrun the shock, prohibiting the formation of a sustained pair-Alfvén shock. This aligns with theoretical expectations for the firehose instability threshold, which constrains the allowable thermal anisotropy at high plasma beta. The simulated cases with $\omega_c = 0.4$ and 0.8 appear to lie near or beyond this stability limit, quenching the waves required to mediate the shock.

Since in the $\omega_c = 0.4$ case, one finds $M_A = 3.54/4 < 1$, but the shock still forms, one concludes that $M_A < 1$ by itself is not a sufficient condition to prevent shock formation. For the waves to escape upstream and, hence, not form a pair-Alfvén shock, the (non-relativistic) condition is $v_A > (v_d + v_{\text{shock}})$ or $M_A < 1 - (v_{\text{shock}}/v_A)$.

The plots in Fig. 5 concisely exhibit the three regimes of instability growth (in the 1D case): weak, intermediate, and strong. The sharpness (or absence) of the shock front, concentration of magnetic energy, and momentum distribution of the charged particles are all clearly distinguished. As we explain, these differences are a result of the ability of the Alfvénic turbulence to outrun the shock as well as the dependency of the relevant plasma instabilities on the difference between the momentum distribution functions in the directions parallel and perpendicular to the background field, or equivalently the shock propagation direction.

The detailed structure in 2D is shown in Figs. 7 and 9, where we see clear formation of a shock front with x-aligned normal in only the weak case. Contrarily, the strong field case has relatively diffuse magnetic energy, of which a significant fraction occupies oblique modes.

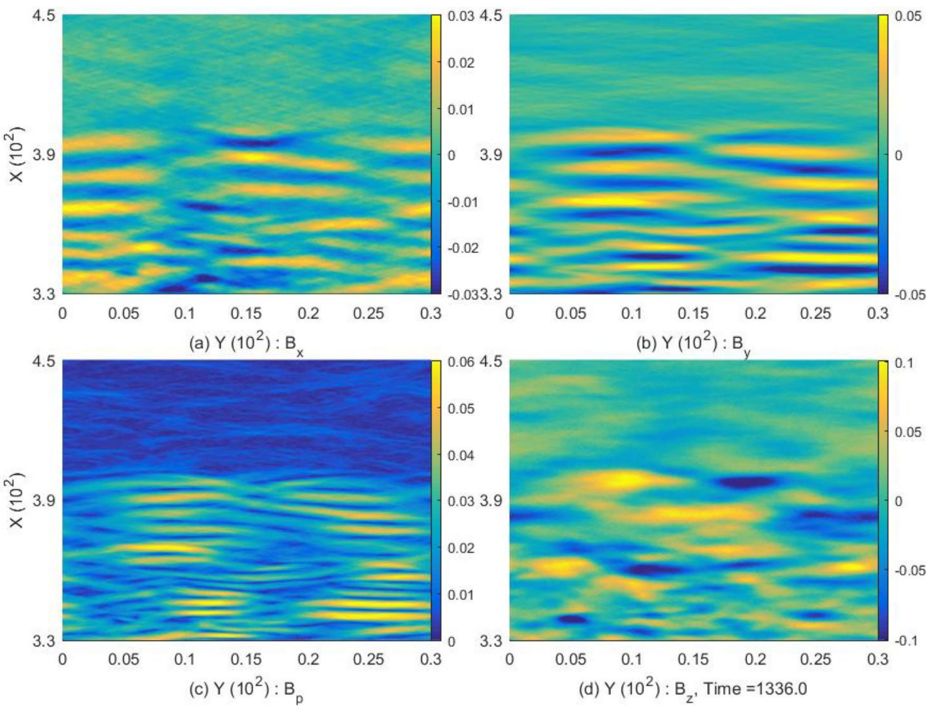

FIG. 9. Magnetic field distribution near the shock for $\omega_c = 0.8$ and $t = 1336$: (a) the magnetic B_x component. (b) B_y. (c) $B_p = ((B_x - B_0)^2 + B_y^2)^{1/2}$ and (d) B_z. Note that in this case, the magnitude of the magnetic field is much smaller than B_0.

The relevant constraints on anisotropy Figs. 2 and 3 are not satisfied here and so the plasma remains non-thermal, as shown in Fig. 6.

The three cases considered in this work ($\omega_c = 0.2, 0.4, 0.8$) of, respectively, weak, moderate, and strong background fields are ultimately distinguished by tendency to equilibrium. Specifically, the weak field case ($\omega_c = 0.2$) shows rapid evolution toward equilibrium, the moderate field case ($\omega_c = 0.4$) evolves more slowly, and the strong field case ($\omega_c = 0.8$) exhibits no clear evolution toward equilibrium. This resolves our questions raised in our previous work,[5] where we had started by examining the formation of the pair-Alfvén shock in the weak case.

Notably, our 2D simulations reveal the presence of oblique Alfvén modes not captured in 1D. However, these oblique waves are still suppressed at high magnetizations and do not lead to shock growth. The oblique modes propagate too slowly to outrun the expanding downstream plasma for the strong field case. The absence of the shock was noted in Ref. 24. We can now explain this since the magnetization is outside the allowed range we identified.

Since these shocks are potentially found across a wide variety of high-energy astrophysical environments, our result is potentially relevant to observational studies of shock emission in high-energy environments. In particular, we have provided an upper limit on the strength of the magnetic field, above which no shock will form. If a pair-Alfvén shock can be identified observationally, one could then conclude an upper limit on the magnetization, $\omega_c \leq 0.8$, which can constrain such predictions as models of jet launching. Additionally, the numerical data produced by the simulations in this work could be used as the background to a radiative transfer code, which could then produce a direct prediction about potential observable signatures for pair-Alfvén shocks. We leave this to a follow-up work.

Here, we have demonstrated the existence of pair Alfvén shocks for a specific set of fiducial plasma parameters, chosen to be representative of high-energy environments such as jets in black-hole microquasars. The results obtained are relevant for shocks with similar formation mechanism in different regimes, subject to similar constraints as considered here. In particular, (i) the shock speed must be fast enough to overtake a significant fraction of the upstream turbulence, (ii) the anisotropy condition for the pair plasma must be satisfied in order to produce the Alfvénic turbulence, and (iii) the temperature must not be so high that our assumptions about the dispersion relation are violated, and other wave modes dominate.[16] Although our current analysis used only a weakly relativistic plasma, this is not a restriction of the simulation code (EPOCH). This investigation could, therefore, straightforwardly be extended to the highly relativistic regimes, which may be expected further along the jet.

The existence of a well-defined Alfvén mode requires a minimum magnetization, corresponding to $\omega_c \sim 0.1$. As can be seen in Fig. 3 (left panel), as the magnetization decreases, resonant interaction with thermal electrons damps the waves, and the spectrum becomes noisy. In this scenario, there is no clear, dominant single Alfvén mode. We point out that low magnetization corresponds to high Alfénic Mach number. On the other extreme, we showed that for magnetization corresponding to $\omega_c \gtrsim 0.4$, the Alfvénic Mach number becomes smaller than unity, and pair-Alfvén shock is suppressed. Our results therefore constrain the minimum magnetization that leads to a clear Pair-Alfvén shock.

We defer to future work the question of whether 3D PIC simulation studies will show whether pair-Alfvén wave could replace the filamentation mode in a realistic geometry. Furthermore, 3D simulations can determine whether pair-Alfvén waves keep their linear polarization in the nonlinear regime. If such shock is to be considered as acceleration sites for cosmic rays, then a population of heavy particles (e.g., protons) can be added to the simulations to see if they are efficiently accelerated and if the presence of these particles and their draw of energy from the shock affects its formation and structure.

ACKNOWLEDGMENTS

The authors also wish to acknowledge the DJEI/DES/SFI/HEA Irish Centre for High-End Computing (ICHEC) for the provision of computational facilities. Derived data supporting the findings of this study are available from the corresponding author upon reasonable request.

AUTHOR DECLARATIONS

Conflict of Interest

The authors have no conflicts to disclose.

Author Contributions

J. D. Riordan: Conceptualization (equal); Data curation (equal); Formal analysis (equal); Investigation (equal); Resources (equal); Visualization (equal); Writing – original draft (equal); Writing – review & editing (equal). **M. E. Dieckmann:** Conceptualization (equal); Data curation (equal); Resources (equal); Software (equal); Supervision (equal); Visualization (equal); Writing – review & editing (equal). **A. Pe'er:** Supervision (equal); Validation (equal); Writing – review & editing (equal).

DATA AVAILABILITY

The data that support the findings of this study are available from the corresponding author upon reasonable request.

REFERENCES

[1]H. Joachim Blome and W. Kundt, "Leptonic jets from young stellar objects?," Astrophys. Space Sci. **148**, 343–361 (1988).
[2]M. Böttcher, M. Pohl, and R. Schlickeiser, "Transrelativistic pair plasmas in AGN jets," Astropart. Phys. **10**, 47–68 (1999).
[3]M. E. Dieckmann, D. Folini, I. Hotz, A. Nordman, P. Dell'acqua, A. Ynnerman, and R. Walder, "Structure of a collisionless pair jet in a magnetized electron-proton plasma: Flow-aligned magnetic field," Astron. Astrophys. **621**, A142 (2019).
[4]M. J. Rees and P. Meszaros, "Unsteady outflow models for cosmological gamma-ray bursts," Astrophys. J. Lett. **430**, L93 (1994).
[5]M. E. Dieckmann, J. D. Riordan, and A. Pe'er, "Change of a Weibel-type to an Alfvénic shock in pair plasma by upstream waves," Phys. Plasmas **27**, 062107 (2020).
[6]A. Marcowith, A. Bret, A. Bykov, M. E. Dieckman, L. O. Drury, B. Lembège, M. Lemoine, G. Morlino, G. Murphy, G. Pelletier, I. Plotnikov, B. Reville, M. Riquelme, L. Sironi, and A. S. Novo, "The microphysics of collisionless shock waves," Rep. Prog. Phys. **79**, 046901 (2016).
[7]A. Bret and R. Narayan, "Density jump as a function of magnetic field strength for parallel collisionless shocks in pair plasmas," J. Plasma Phys. **84**, 905840604 (2018).
[8]M. E. Dieckmann, D. Folini, A. Bret, and R. Walder, "Simulation studies of temperature anisotropy driven pair-Alfvén and aperiodic instabilities in magnetized pair plasma," Plasma Phys. Controlled Fusion **61**, 085027 (2019).
[9]A. R. Bell, "Turbulent amplification of magnetic field and diffusive shock acceleration of cosmic rays," Mon. Not. R. Astron. Soc. **353**, 550–558 (2004).
[10]M. A. Riquelme and A. Spitkovsky, "Nonlinear study of Bell's cosmic ray current-driven instability," Astrophys. J. **694**, 626 (2009).
[11]G. Pelletier, "Fermi acceleration of astroparticles," in *Physics and Astrophysics of Ultra-High-Energy Cosmic Rays* (Springer Berlin Heidelberg, Berlin, Heidelberg, 2001), pp. 58–89.
[12]M. Linares and M. Kachelrieß, "Cosmic ray positrons from compact binary millisecond pulsars," J. Cosmol. Astropart. Phys. **2021**, 030.
[13]L. Sironi, U. Keshet, and M. Lemoine, "Relativistic shocks: Particle acceleration and magnetization," Space Sci. Rev. **191**, 519–544 (2015).
[14]L. Sironi and A. Spitkovsky, "Particle acceleration in relativistic magnetized collisionless pair shocks: Dependence of shock acceleration on magnetic obliquity," Astrophys. J. **698**, 1523–1549 (2009).
[15]D. J. Stark, L. Yin, B. J. Albright, and F. Guo, "Effects of dimensionality on kinetic simulations of laser-ion acceleration in the transparency regime," Phys. Plasmas **24**, 53103 (2017).
[16]R. Keppens, H. Goedbloed, and J.-B. Durrive, "Waves in a warm pair plasma: A relativistically complete two-fluid analysis," J. Plasma Phys. **85**, 905850408 (2019).
[17]A. Bret and R. Narayan, "Density jump for parallel and perpendicular collisionless shocks," Laser Part. Beams **38**, 114–120 (2020).
[18]A. Bret and R. Narayan, "Density jump as a function of magnetic field for switch-on collisionless shocks in pair plasmas," J. Plasma Phys. **88**, 905880320 (2022).
[19]A. Bret, "Density jump as a function of magnetic field strength for parallel collisionless shocks with anisotropic upstream pressure," Mon. Not. R. Astron. Soc. **520**, 6083–6090 (2023).
[20]O. Pokhotelov, R. Sagdeev, M. Balikhin, and R. Treumann, "Mirror instability including finite Larmor radius effects," Adv. Space Res. **37**, 1550–1555 (2006).
[21]T. D. Arber, K. Bennett, C. S. Brady, A. Lawrence-Douglas, M. G. Ramsay, N. J. Sircombe, P. Gillies, R. G. Evans, H. Schmitz, A. R. Bell, and C. P. Ridgers, "Contemporary particle-in-cell approach to laser-plasma modelling," Plasma Phys. Controlled Fusion **57**, 113001 (2015).
[22]C. K. Birdsall and A. B. Langdon, *Plasma Physics via Computer Simulation* (McGraw-Hill, 1985), p. 479.
[23]G. Livadiotis, "Shock strength in space and astrophysical plasmas," Astrophys. J. **809**, 111 (2015).
[24]A. Bret, A. Pe'er, L. Sironi, A. Sadowski, and R. Narayan, "Kinetic inhibition of magnetohydrodynamics shocks in the vicinity of a parallel magnetic field," J. Plasma Phys. **83**, 715830201 (2017).